Aeroacoustics Conferences
26-29 May 2026, Brussels, Belgium
32nd AIAA/CEAS Aeroacoustics Conference (2026)

10.2514/6.2026-3389

Aeroacoustic Test Bench Characterization of the TUC-TUC Rotor in Hover Flight

Isaac S. Bensignor*, Lourenco Tercio Lima Pereira†, and Daniele Ragni ‡
Delft University of Technology, Kluyverweg 1 2629HS Delft Netherlands

The TU Delft Characterization model for roTor aeroacoUstiCs (TUC-TUC) is a modular rotor test bench developed for controlled aerodynamic and acoustic characterization under simplified and well-defined conditions. The platform permits systematic variation of blade pitch and airfoil type and is intended to support the study of rotor aeroacoustic behavior in a more interpretable manner than is typically possible with conventional rotor geometries. This paper presents the commissioning and initial hover characterization of TUC-TUC in the A-Tunnel facility at TU Delft using integral load measurements, acoustic directivity measurements, and particle image velocimetry of the flow field. The measurements are complemented by performance estimates from a blade element momentum theory model coupled with a harmonic source formulation. The results show that the measured aerodynamic response is captured well in trend and magnitude by the performance model, despite an apparent pitch-angle offset between predictions and experiments. The acoustic measurements are likewise found to be broadly consistent with the intended design criteria, including expected velocity scaling and clear source separation between the outer test section and inner structure. Taken together, the results establish TUC-TUC as a suitable basis for continued aerodynamic and aeroacoustic characterization and for future study of rotor-noise mechanisms under controlled conditions.

I. Nomenclature

A = Disk area, m^2
B = Number of blades
C_l = Lift coefficient
C_P = Pressure coefficient
C_T = Thrust coefficient
C_Q = Torque coefficient
D = Rotor diameter, m
FM = Figure of merit
F_Z = Axial force, N
f = Frequency, Hz
k_{95} = 95% uncertainty confidence bound
M = Mach number
M_Z = Moment about axial force axis, Nm
m = Hamonic number
n = Critical amplification factor
Q = Moment (torque) load, $N\,m$
Q_0 = Drift compensated torque load, $N\ m$
R = Microphone arc radius, m
Re = Chord Reynolds number
R_b = Blade radius, m
T = Temperature, $^\circ C$
T = Thrust force, N
T_0 = Drift compensated thrust force, N
t = Time, s
U_∞ = Freestream velocity
U, V = Flow velocity (components), m/s
x/c = Non-dimensional chord length
Γ = Bound circulation, m^2/s
ε_x = Expanded 95% confidence uncertainty
ϵ_x = Uncertainty of "x"
θ = Observer angle relative to the rotor axis, deg
ρ_0 = Ambient air density, kg/m^3
σ = Rotor solidity
Ω = Rotational speed, $1/s$
∞ = Freestream denotation

*PhD Candidate, Aeroacoustics - Flow Physics and Technology Department, AIAA Member.
†Assistant Professor, Aeroacoustics - Flow Physics and Technology Department, AIAA Member.
‡Associate Professor, Aeroacoustics - Flow Physics and Technology Department, AIAA Member.

II. Introduction

A. Motivation and Background

In recent years, rotor aeroacoustics has received increasing attention because of the need to better understand and predict the noise generated by small-scale propellers and rotors. At these scales, where blade geometries are compact, rotational speeds are high, and operating Reynolds numbers are low ($Re \leq O(10^5)$), rotor aeroacoustic behavior becomes increasingly difficult to characterize in a consistent and transferable way. Under such conditions, the measured response is sensitive to operating condition, geometry, installation, and local flow development, all of which can be difficult to control or reproduce experimentally. This challenge is compounded by the practical difficulty of analyzing conventional rotor blades, whose geometries typically contain multiple coupled features such as twist, taper, sweep, chord variation, and section changes. These complexities, together with uncertainties in manufacturing precision and installation, make it difficult to determine how individual blade characteristics influence the measured acoustic response. Instead, the measured response reflects the combined effects of operating condition, blade geometry, three-dimensional flow development, and installation-dependent interactions.

Recent experimental and numerical studies have accordingly examined effects such as multi-rotor or distributed-rotor positioning and phase synchronization [1, 2], as well as installation effects associated with nearby structures and aerodynamic interactions [3–5]. Although these investigations provide important insight, they also underscore the difficulty of isolating the fundamental aerodynamic and acoustic mechanisms governing the measured response. This challenge is further reflected in the discrepancies that remain between experimental measurements and rotor-noise predictions in the low-Reynolds-number regime [6]. Consequently, there remains a need for simplified and well-controlled experimental platforms that can provide fundamental data for model validation and more interpretable aeroacoustic analysis. Improved understanding is therefore needed of how low-Reynolds-number flow conditions influence the measured response, particularly through experiments in which the configuration is controlled as tightly as possible and, where full control is not possible, the flow field is measured in sufficient detail to enable physically meaningful interpretation.

TUC-TUC, detailed in the next section, was developed in response to this need as a simplified rotor platform for aeroacoustic characterization. The platform was conceived to reduce geometric complexity and thereby improve the interpretability of the measured response relative to conventional rotor configurations. In this way, changes in pitch, rotational speed, and loading can be assessed under controlled conditions and related directly to the measured aerodynamic and acoustic response. Such control is also important because aeroacoustic experiments can be affected by rig- and facility-dependent influences, including recirculation, model asymmetry, and unsteady loading introduced by the surrounding structure or support hardware, which can obscure the true source characteristics. These effects may appear as biases in the sound pressure level (SPL) at the blade-passing frequency (BPF) and its harmonics, as well as changes in the measured directivity. Within this context, a deliberately simplified and modular platform provides a more interpretable basis for relating operating-condition changes to far-field noise, integral performance, and measured flow-field quantities, while also supporting comparison with analytical and physics-based prediction methods.

The present work focuses on the commissioning and characterization of TUC-TUC. It presents a summary of the TUC-TUC design and supporting test methodology, followed by the initial hover characterization of the platform through integral load measurements, acoustic directivity measurements, PIV-based flow-field measurements, and comparison with blade element momentum theory (BEMT)/Hanson-based predictions. The paper concludes with a summary of the commissioning results and an outline of ongoing and future work.

B. A Test Bench System for Assessing Fundamental Rotor Aeroacoustics: TUC-TUC

TUC-TUC – the **TU** Delft **C**haracterization model for ro**T**or aeroaco**U**sti**C**s – is a simplified rotor platform developed for detailed aeroacoustic investigation. TUC-TUC's design and performance estimates were first introduced in Bensignor *et al.* [7], but is presented herein with additional details and experimental performance results. For the reader's benefit, details of TUC-TUC are summarized. TUC-TUC is a dedicated test bench for enhancing the measurability and separability of different blade-characteristic contributions to radiated noise. The platform is intended to support the study of tonal loading noise, thickness noise, blade-wake interaction, blade-vortex interaction, and directivity changes associated with (unsteady) blade loading. TUC-TUC's design facilitates controlled studies that can directly link the flow field to acoustic emissions, serving as a validation experiment for analytical formulations and physics-based models. In conventional experimental setups, such effects are often difficult to isolate or quantify because of geometric complexity. Thus, none of the classic performance enhancing features like, for example, spanwise twist, sweep, or optimizing the tip shape are implemented. The efficiency of TUC-TUC in terms of thrust, torque or figure of merit are also not relevant to the scope of this research effort (however, they are measured and estimated). The physical layout and key design features of TUC-TUC are shown in Fig. 1. The inner-airfoil-only configuration of TUC-TUC, used to assess the impact of the remaining structure on the test airfoil (i.e., the self-background noise), is shown in Fig. 2.

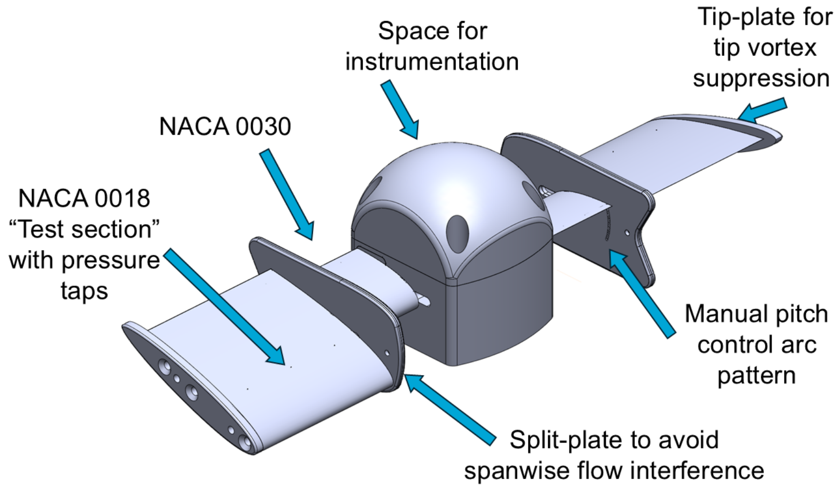

Fig. 1 The TUC-TUC system, showing its salient design features and characteristics.

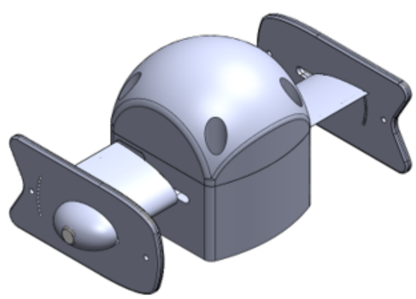

Fig. 2 Inner TUC-TUC test configuration (without test section airfoil).

TUC-TUC was also conceived as a modular test bench, allowing its components to be swapped or removed so that different geometries and configurations can be assessed. The current configuration features a NACA 0018 "test section" airfoil and a NACA 0030 structural support "inner" airfoil. The test section and inner airfoil are both of aspect ratio equaling 1, with a chord of 90 and 45 mm, respectively.

Hubbard *et al.* [8] and Lowson and Ollerhead [9] discuss noise-velocity scaling laws for propellors and rotors. Relying on these, the sizing and choice of TUC-TUC's current components were determined. The signal-to-noise ratio (SNR) of the outer-to-inner airfoil sections were chosen to be 27 and 18 dB when assuming a Ω^6 and Ω^4 acoustic power scaling assumption for loading and thickness noise, respectively. The SNR quantities are for a design speed of 6,000 RPM (200 Hz). This rotation frequency relates to the cut-off frequency of the acoustic-treated wind tunnel TUC-TUC is operated in [10] and is also the BPF first harmonic.

Both the test section and inner airfoil can be pitched independently of one another using guide angle arcs situated in the mid-plates and hub. This feature allows the inner airfoil angle to be set such that for non-hover conditions, the angle corresponding to minimum loading (and thus a minimum in noise) can be used for the corresponding axial or edgewise flight. With such a capability, the self-background noise contribution can be reduced optimally for each test scenario. The current configuration allows for the test section and inner airfoil to have a pitch angle resolution of 2 and 2.5 degrees, respectively. Given the independent degrees of freedom of the pitching components, the terms rotor and propeller are used interchangeably in the context of TUC-TUC. The design speed, mid-test section span Reynolds number, and tip Mach number, along with other pertinent details are noted in Table 1. Moreover, the diameter, hub, and solidity, along with other critical additional geometric characteristics of TUC-TUC are reported in Table 2.

There are two notable spanwise discontinuities in TUC-TUC's design: a mid-plate and a tip plate. The mid-plate's design was informed by NACA reports on the hydrodynamics of airfoils with end plates as reported by Wadlin *et al.* [11]. The mid-plate serves as a means of pitching the airfoils independently, as they are a physical reference anchor, and to prevent the formation of spanwise flow gradients. Moreover, a tip plate is incorporated to mitigate the effects of the tip vortex and reduce associated flow-induced losses.

Table 1 Design test conditions and characteristics.

Rotation speed	6,000	RPM
Blade passing frequency	200	Hz
V_{tip}	113	$\frac{m}{s}$
Re (Outboard mid-span)	4.8×10^5	
Tip Mach number	0.33	
Tip dynamic pressure	7,600	Pa

Table 2 TUC-TUC geometric characteristics.

Diameter	360.0	mm
Number of blades	2	
Solidity, $\sigma = \frac{A_{Blades}}{A_{Disk}}$	0.216	
Hub radius	36.0	mm
NACA 0030 chord	45.0	mm
NACA 0030 pitch range	-20 : 2.5 : 20	deg
Mid-plate chord	105.0	mm
Mid-plate span width	4.0	mm
Mid-plate max. thickness	54.0	mm
NACA 0018 chord	90.0	mm
NACA 0018 pitch range	-20 : 2 : 20	deg
Tip plate chord	99.0	mm
Tip plate span width	5.0	mm
Tip plate max. thickness	17.8	mm
Unbalanced rotor mass	1.34	kg

III. Experimental Setup and Methods

TUC-TUC was tested in the Delft University of Technology's Anechoic Wind Tunnel Facility (A-Tunnel) [10]. Tests were realized at ~6,000 RPM with pitch angles varying from 0° to 20° in steps of 4°. The inner-only configuration was also measured at the same speed. An example schematic of the setup can be found in Fig. 3a and the internal structure and select components is shown in Fig. 3b. A cylindrical nozzle inlet is used in the experiments with a diameter of 600 mm ($1.66D$), and the Rotor Rig is placed at zero degrees angle of attack relative to it. The Rotor Rig internal components are covered by a 3D-printed nacelle intended to streamline the flow and minimize aerodynamic interferences. Two wing structures, 400 mm ($1.11D$) downstream from the rotor disk, support the rig. This distance is deemed far enough to consider the setup unobstructed with respect to effects as if treated as ground interference [12]. A Hacker Q80-6L V2 kV 180 motor and a Silixcon 18 kW electronic speed controller are used to drive the propeller.

Prior to testing, a Schenk SmartBalancer was used to balance TUC-TUC for each test condition. A balancing grade of G6.3 was achieved, as specified for small propellers according to ISO 21940-11-2016 [13], which allows for permissible residual imbalance up to 15 g mm. Across the tested configurations, the vibration magnitude ranged from 3.20 to 5.43 mm/s, while the corresponding permissible residual imbalance ranged from 7.7 to 11.5 g mm. For the TUC-TUC configuration specifically, the minimum vibration magnitude occurred at 0° pitch (3.20 mm/s) and the maximum at 12° pitch (4.48 mm/s), with corresponding permissible residual imbalance levels of 7.7 and 11.5 g mm, respectively. Figure 4 illustrates the first-order effect of rotor balancing on the measured acoustic spectra. The unbalanced configuration highlights the influence of balancing on the SPL at the BPFs and shaft harmonics.

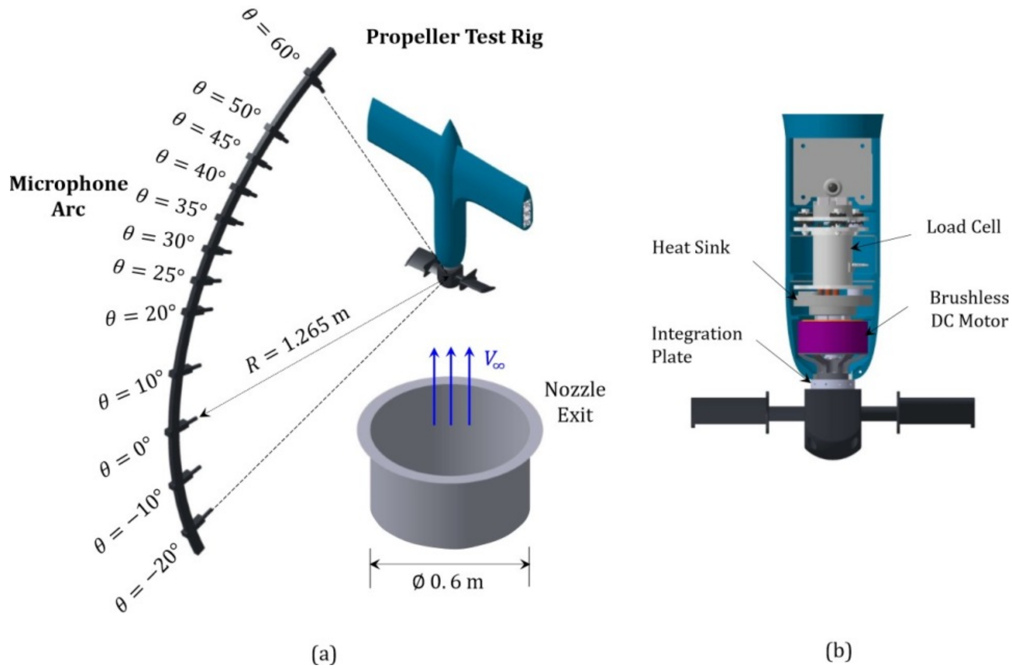

Fig. 3 Example depiction of microphone arc and rotor rig.

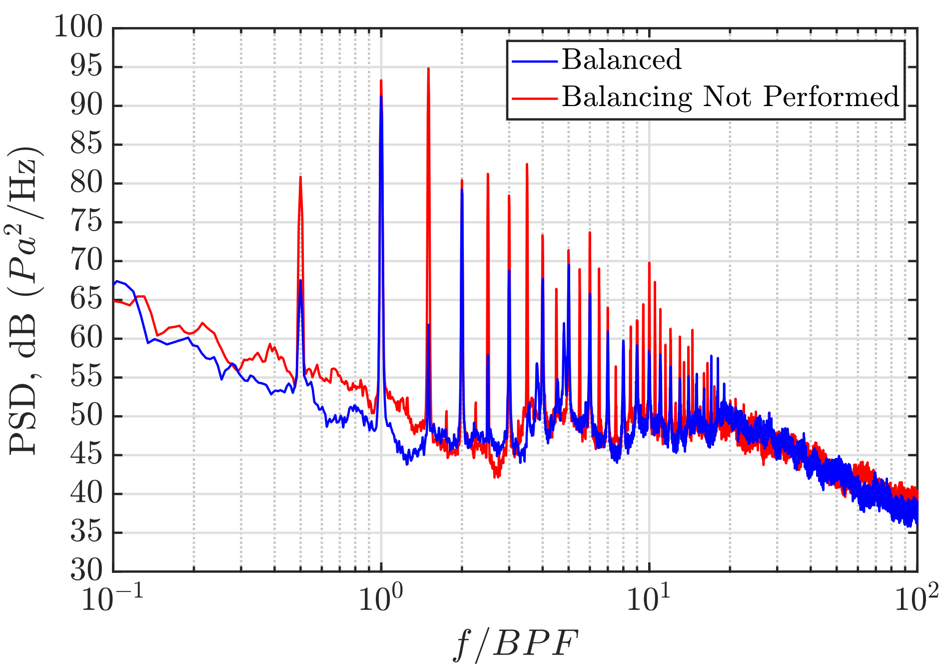

Fig. 4 Exemplary balancing procedure impact on measured (unfiltered) spectra of 16° pitch at 6,000 RPM for the 40° microphone.

A. Instrumentation and Data Acquisition

1. Integral Load Measurements

Two different load cells characterized TUC-TUC's response, with the latter demonstrating reduced uncertainty in the load measurements taken. The first was a 6-axis ATI Mini-45, rated for 290 N and 10 Nm, where thrust and torque reported corresponded to the Z-axis force and Z-axis moment. The calibration certificate reports maximum measurement uncertainties at the 95% confidence level of 0.75% of full scale for F_z and 1.25% of full scale for M_z. The second instrument was a FUTEK MBA500 bi-axial load cell rated for 444 N and 11.2 N m with a IAA100 amplifier. The sensor has a non-linear rated output (RO) tolerance of 0.25%, and a temperature drift of 0.01% of the RO per $^\circ C$. The average uncertainty across the test matrix are reported in Table 3. Percentage uncertainties for thrust and torque are normalized by the approximate maximum measured loads, $T_{\max} \approx 40$ N and $Q_{\max} \approx 2$ N m.

Table 3 Average uncertainties quantified.

Load Cell	ε_T $[N]$	$\varepsilon_T/T_{\max}$ [%]	ε_{C_T} [-]	ε_Q $[N\ m]$	$\varepsilon_Q/Q_{\max}$ [%]	ε_{C_Q} [-]
ATI	±4.35	±10.9	$\pm 2.8 \times 10^{-3}$	±0.13	±6.5	$\pm 4.45 \times 10^{-4}$
FUTEK	±1.85	±4.6	$\pm 1.2 \times 10^{-3}$	±0.05	±2.5	$\pm 1.60 \times 10^{-4}$

The average expanded uncertainties of ±1.85 N in thrust and ±0.05 N m in torque are within the range reported for small-scale rotor and propeller experiments. Cai and Gunasekaran [14] reported average force and torque uncertainties of 9.4% and 7.2%, respectively, for a small fixed-pitch propeller, such that the FUTEK measurements compare favorably. Wu et al. [15] reported 95% confidence thrust and torque uncertainties of 0.084 N and 0.873 N mm, respectively, for a 217.2 mm benchmark propeller, which are lower in absolute magnitude but correspond to a different propeller scale and loading range. Overall, the FUTEK measurements exhibits uncertainty levels that are competitive for subscale rotor testing, with the torque uncertainty in particular comparing well against the broader literature. Additional details related to the uncertainty characterization performed for the load cell data reduction can be found in Appendix A.

2. Flow Field Measurements

Particle image velocimetry (PIV) measurements were performed to characterize the local flow field around TUC-TUC. Results from the 12 degree pitch at 6,000 RPM test case are presented below. The location of the mid-span plane of the NACA 0018 imaged is furthest from any spanwise geometric discontinuity. Here, ideally, the flow is expected to be quasi-2D, which can allow for a comparison to BEMT/XFOIL predictions.

A planar, dual-pulse, phase-locked PIV setup was used [16]. Two Imager sCMOS LaVision cameras were arranged such that their field of view cover both suction and pressure sides of the blade. The cameras have 2560x2160 pixel resolution and are two image interframing capable. A Quantel Evergreen 200 mJ laser is used with LaVision DaVis and a timing unit for trigger/laser pulse synchronization and data acquisition. The laser sheet was measured to be approximately 1 mm thick, and was split via a partitioning mirror such that the suction and pressure side was illuminated. A small shadow region persisted near the trailing edge in the merged field of view. The wind tunnel was seeded with SAFEX-Inside-Nebelfluid using a SAFEX Twin Fog generator, which produces particles approximately 1 micrometer in diameter.

Optical access was limited during the test due to the supporting structure. Therefore, the cameras and the laser were placed 60° from each other, rather than in orthogonal planes. Because the cameras viewed the measurement plane obliquely, Scheimpflug adaptors were used to maintain focus across the illuminated light sheet. Calibration of the cameras, image acquisition, and image post-processing was facilitated via LaVision DaVis 11.3. The images were processed using an window iterative multi-grid deformation method, with a final window size of 12x12 pixels and a 75% overlap. Further processing via a median filter removed extraneous vectors and were subsequently replaced via an interpolation schema. The reported flow field is presented in the blade's non-inertial frame, such that the rotational speed is subtracted from the U-velocity field imaged. Further details of the setup and post-processing parameters are detailed in Table 4.

Table 4 Details of PIV setup.

Imaging parameters		PIV processing	
Camera	2 Imager sCMOS	Software	LaVision Davis 11.3
Number of pixels [px]	2,560 × 2,160	Pulse separation [μs]	20
Pixel size [μm^2]	6.5 × 6.5	Number of recordings	2,000
Focal length [mm]	105	Minimum window size [px^2]	12 × 12
Magnification	0.07		
Imaging resolution [$\frac{px}{mm}$]	≈ 10		
FOV [cm^2]	≈ 25.5 × 28.1		
Spatial resolution [mm]	≈> 0.25		
f#	8		

3. Acoustic Measurements

A microphone arc is placed parallel to the rotation axis of TUC-TUC, outside of the flow region. The arc is comprised of eight GRAS 46BE and three GRAS 40PH microphones installed radially at 1.265 m from the central hub of TUC-TUC. The microphones are ±1 dB accurate in the measurement frequency range of interest (< 20 kHz). The directivity angles of the GRAS 46BE microphones vary from -20° to +60° in 10° steps, and the three GRAS 40PH were placed at 25°, 35°, and 45 °. The microphone at 0° sits in the same horizontal plane of rotation as the rotor. Additionally, an NI PXIe4499 acquired data from the microphones, load cell, and once-per-revolution magnetic hall encoder sensor at a rate of 204,800 samples per second for 20 seconds.

To remove spurious and very low frequency noise, a high pass filter removed all sub-shaft frequency content. To enable obtaining the SPL for the BPFs, a Vold-Kalman filter (VKF) of 2nd order with 10 Hz bandwidth removed selected harmonics of the shaft frequency from the pressure-time signal. From this cleaned signal, a second VKF was implemented to isolate the tonal harmonics above the broadband residual, according to each spectrum. Subtracting the filtered pressure tonal signal from the cleaned pressure signal yielded the broadband signal. The filtered tonal data was ±10 Hz bandpassed to isolate further the individual tones, when presented as a single SPL value (normalized by 2×10^{-5} Pa). The time-pressure signals acquired via the microphones were processed with a Welch autocorrelation to obtain power spectral density [17]. A block size of 65,536 (2^{16}), a Hanning window and 0.5 overlap window were used. The frequency spectra are presented in terms of power spectral density, have units of decibels, and are normalized by a reference of 4×10^{-10} Pa^2/Hz. The frequency axis is normalized by each tests' respective BPF, where BPF is determined each case based on the hall effect sensor data acquired synchronously.

B. Performance Estimates via Blade Element Momentum Theory and Hanson's Formulation

A BEMT model was coupled with a numerical implementation of Hanson's harmonic source formulation [18] to allow for a comparison to the measured loads and noise. The BEMT model is based on Leishman's [12] formulation and the non-dimensionalized performance coefficients are presented in the US customary helicopter convention in Eqs. 1-3. The BEMT implementation models only the NACA 0018 and tip plate as force producing spanwise elements. Additionally, the tip plate is treated like an extension of the NACA 0018 given its geometric similarity. Measurement of the inner-structure-only configuration at the design condition were used as a torque offset with the assumption of independent superposition of loads, i.e. no aerodynamic interference between inner and outer blade sections. Prandtl's tip and root loss correction is implemented to account for finite span effects.

$$C_T = \frac{T}{\rho_o \Omega^2 R_b^2 A}. \tag{1}$$

$$C_Q = \frac{Q}{\rho_o \Omega^2 R_b^3 A}. \tag{2}$$

$$FM = \frac{C_T^{3/2}}{\sqrt{2} C_Q}. \tag{3}$$

The airfoil performance data used in the BEMT predictions was generated via XFOIL for both free e^n transition (n = 9, given by Mack's relationship for a turbulence intensity of 0.07% [10]) and forced transition at x/c = 10%. The Prandtl-Glauert correction was applied to account for Mach effects. An implementation of Hanson's formulation by Goyal *et al.* [19] was modified for integration with the BEMT model. A parabolic fit is assumed for the local-chordwise force distribution [18], and the thickness shape distribution comes from model geometry. Tonal noise is estimated via BEMT predicted lift and drag coefficient distributions.

IV. Results and Analysis

A. Aerodynamic Load Characterization

Figures 5 and 6 present the measured thrust and torque coefficients as functions of pitch angle at ~6,000 RPM. The error bars denote the 95% confidence bounds determined for each test case. Repeated data points at a given pitch angle arise from overlap between the different load measurements acquired. Estimated performance is shown for both free-e^n transition and forced transition at x/c = 10%. In both figures, the shaded "Isolated Inner Structure" region denotes the contribution of the inner structure measured. For the torque coefficient, this measured inner-structure contribution is applied as an offset to the BEMT predictions in order to account for its torque contribution to TUC-TUC. No corresponding thrust contribution is expected, since the inner structure is held at 0° pitch in the tested configuration.

Overall, the measured trends are consistent with the expected qualitative behavior of a rotor operating in the linear regime. Over the higher-pitch portion of the test matrix, the thrust coefficient increases approximately linearly with pitch angle, while the torque coefficient exhibits a non-linear increase. This is consistent with classical rotor aerodynamic theory [12]. In this sense, the measured response follows the general behavior expected of conventional rotor geometries.

The primary departures from these trends occur at the lowest pitch angles. In the thrust data, the measurements at 0° and 4° do not follow the higher-pitch linear trend, and the thrust measured at 0° is not approximately zero. A similar deviation is present in the torque data, for which the lowest-pitch measurements do not follow the higher-pitch trend and the measured torque at 0° exceeds that at 12°. The exact origin of these low-loading deviations is still under investigation. One possible contributing factor is that, as rotor loading decreases, the relative influence of measurement uncertainty and small parasitic contributions becomes larger with respect to the quantity being measured.

The comparison between measurements and estimates is better understood via Figs. 7 and 8, which present thrust coefficient versus torque coefficient and figure of merit versus thrust coefficient, respectively. In Fig. 7, the predictions closely reproduce both the overall trend and the magnitude of the measurements. This indicates that the underlying aerodynamic behavior is captured well by the model, and suggests that the discrepancy observed in Figs. 5 and 6 is more consistent with an apparent pitch-angle offset than with a deficiency of the modeling approach and physics. The source of this offset, which is on the order of approximately 1–2°, remains under investigation. Overall, the comparison demonstrates good qualitative and quantitative agreement between the measured and predicted rotor performance.

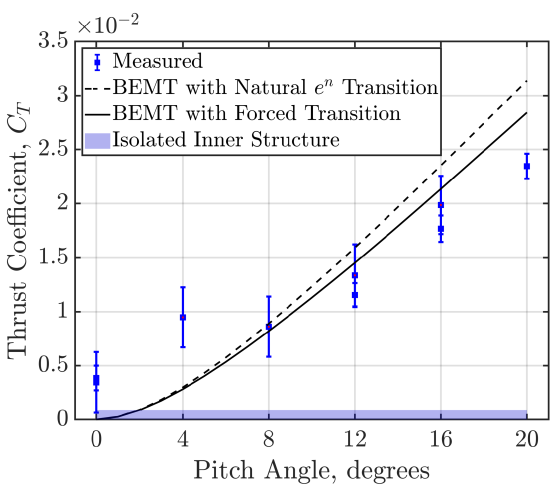

Fig. 5 Measured and estimated thrust coefficient vs. pitch angle at ~6,000 RPM.

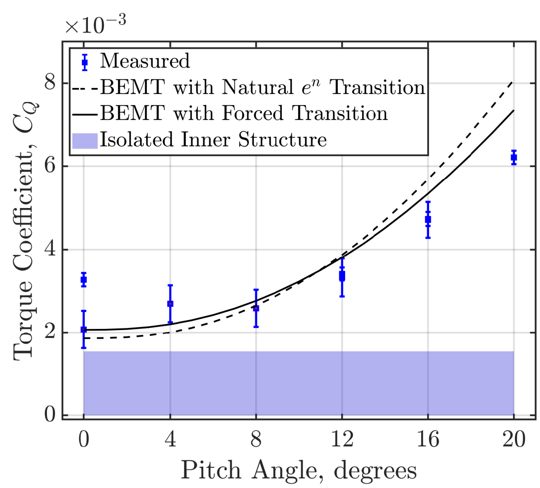

Fig. 6 Measured and estimated torque coefficient vs. pitch angle at ~6,000 RPM.

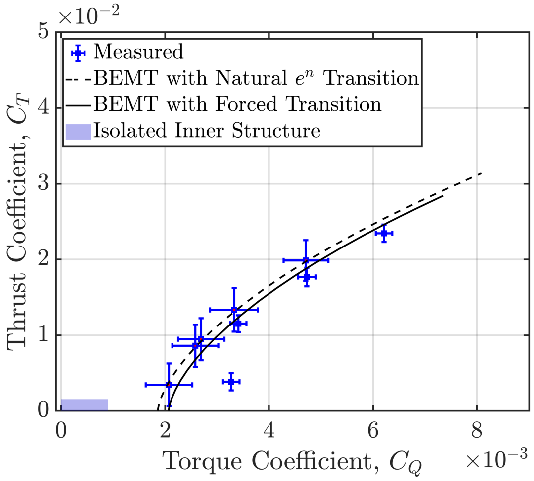

Fig. 7 Measured and estimated thrust coefficient vs. torque coefficient at ~6,000 RPM.

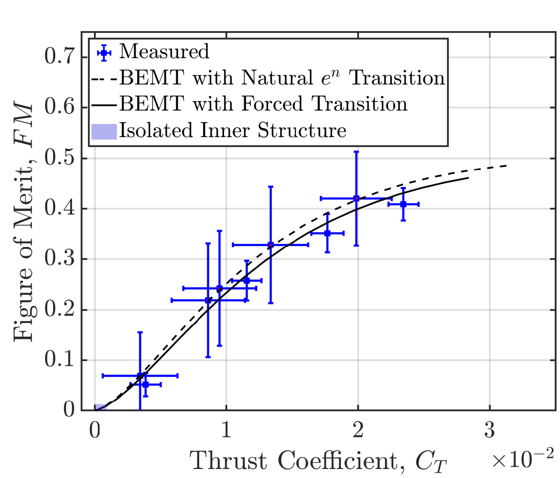

Fig. 8 Measured and estimated figure of merit vs. thrust coefficient at ~6,000 RPM.

Analysis of TUC-TUC's flow field state was performed via a planar PIV setup. A NACA 0018 airfoil profile was positioned in the imaged masked region using the qualitatively best geometric fit. The resulting velocity magnitude field and streamlines shown in Fig. 9 exhibit the expected qualitative behavior of a lifting section at a forward velocity. Notably different from an isolated airfoil flow, a low velocity region below the leading edge, marked region "A," suggests the presence of a nearby flow structure not directly associated with the bound circulation on the section. This flow structure is understood to be a shed vortex from a preceding blade in the rotation phase imaged.

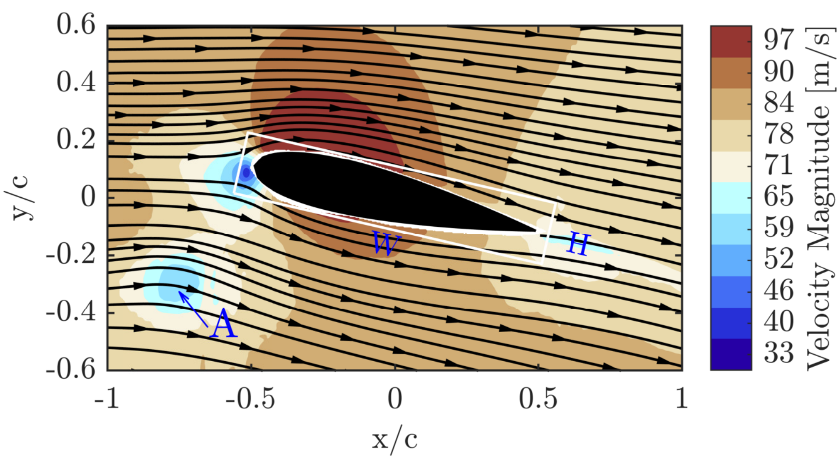

Fig. 9 Mid-span velocity magnitude field and streamlines at 12° pitch and ~6,000 RPM, with representative box denoting the bound circulation region.

The representative rectangular box shown in Fig. 9 denotes the integration region selected for the bound circulation evaluation determined by a convergence trend assessment depicted in Fig. 10. This region was chosen such that the bound circulation around the airfoil was captured while avoiding inclusion of the localized off-body vortex beneath the leading edge. Although clearly present in the measured field, it remains sufficiently separated from the selected contour to avoid contamination when reporting circulation-based quantities. The sensitivity of the circulation estimate to integration-region dimensions is reported in Fig. 10. When the rectangular bounding region height is normalized by airfoil thickness, the mean values of Γ, C_l, and effective angle of attack, α, exhibit a comparatively strong convergence trend, becoming essentially settled by approximately $H/t \approx 1.21$. In contrast, the dependence on normalized bounding region width, W/c, is weaker and does not display a distinct convergence behavior. The selected "best" bounding region was therefore taken as the smallest region for which the mean response had stabilized, that being $W/c = 1.1$ and $H/t = 1.21$.

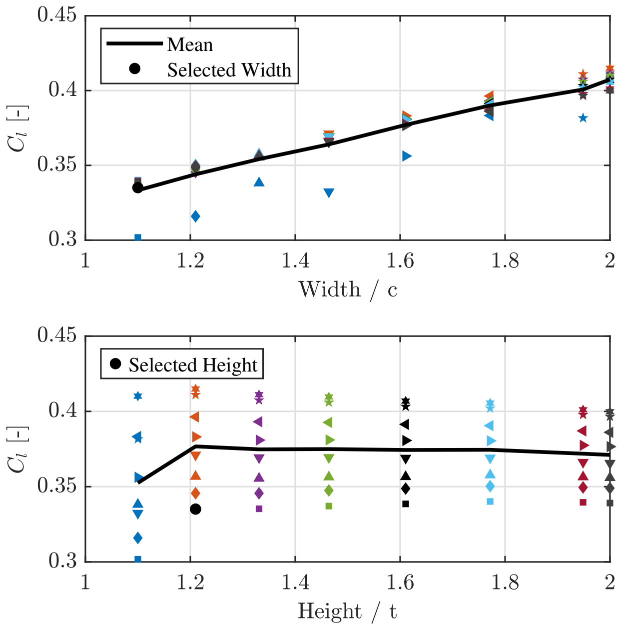

Fig. 10 Convergence trends for varying integration area ratios for circulation-derived lift coefficient.

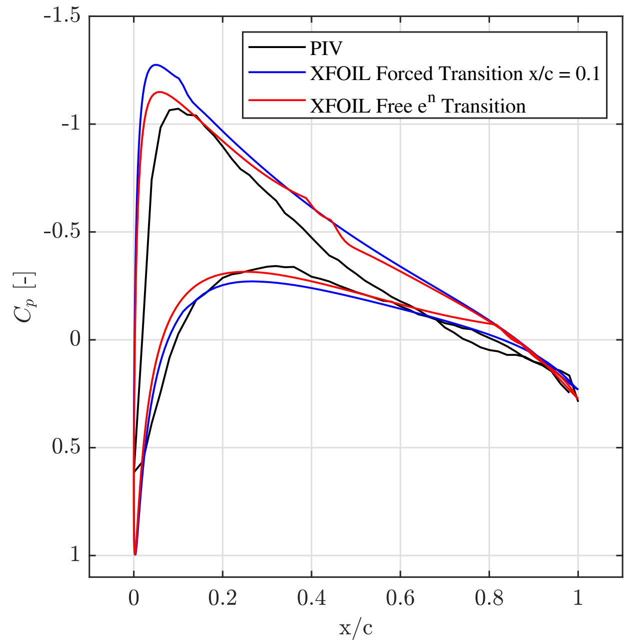

Fig. 11 Measured and estimated pressure coefficient distribution at the mid-section plane of the NACA 0018 airfoil.

The pressure-coefficient comparison in Fig. 11 shows that the PIV-based reconstruction captures the expected qualitative features of a lifting airfoil. Relative to the XFOIL-based distributions, however, the reconstructed suction peak is weaker and displaced farther downstream, which is consistent with a lower effective angle of attack. The measured stagnation C_p also deviates from the theoretical value of unity. In the present method, C_p was not measured directly at the wall, but was inferred from the velocity field using a near-surface nearest-neighbor procedure, since the mask region extended beyond the airfoil profile. For each point along the airfoil profile, the local outward normal was constructed and the first usable off-wall point along that normal was identified. The Cartesian velocity components at that location were then obtained from the PIV field using nearest-neighbor interpolation, yielding the near-surface values U_{surf} and V_{surf}. These were used to estimate the local near-surface velocity magnitude as

$$\bar{V} = \sqrt{U_{\text{surf}}^2 + V_{\text{surf}}^2}. \tag{4}$$

The pressure coefficient was then estimated as

$$C_p = 1 - \left(\frac{\bar{V}}{U_\infty}\right)^2, \tag{5}$$

which implicitly assumes that a Bernoulli relation provides a reasonable approximation between the local near-surface velocity and static pressure.

A comparison of the flow quantities and respective condition estimated is summarized in Table 5. The circulation-based lift coefficient obtained from the bounding region compares favorably with the sectional predictions, albeit XFOIL's relative over-prediction. The PIV-inferred and BEMT/XFOIL predicted section effective angle of attack are within ~1 degree. Overall, the mid-span PIV results support a quasi-two-dimensional interpretation of the section aerodynamics at this operating condition.

The near-wall pressure field remains sensitive to the finite PIV spatial resolution, the extent of the masked region, the placement of the airfoil profile in the captured flow velocity domain, the choice of near-surface velocity estimation method, and the validity of the potential flow assumption. Accordingly, the reconstructed C_p distribution is best interpreted as a qualitative indicator of stagnation-region and suction-peak behavior rather than as a basis for force extraction. This interpretation is consistent with the discrepancy between the lift coefficient obtained from direct integration of the reconstructed C_p distribution and the circulation-based lift estimate.

Table 5 Comparison of airfoil performance metrics.

	Best Found Bounding Region	XFOIL Tripped	XFOIL Free
Γ $[m^2/s]$	1.24	1.58	1.33
C_l	0.34	0.43	0.36
C_l via integration of C_p from nearest neighbor	0.23	–	–
α from $C_{l_{\alpha,\text{tripped}}} = 5.13$ $[deg]$	3.7	3.9	–
α from $C_{l_{\alpha,\text{free}}} = 6.65$ $[deg]$	2.9	–	3.4

B. Measured and Estimated Noise

Figure 12 compares the 0° spectra of the full TUC-TUC configuration with that of the inner-airfoil-only configuration at ~6,000 RPM. This comparison is used to assess the self-noise contribution of the inner structure relative to the full rotor response. The full TUC-TUC configuration exhibits substantially higher noise at the first BPF and its harmonics, indicating that the measured acoustic response is dominated by the outer test section rather than by the inner supporting structure. At 0° pitch, where thickness noise dominates the radiated response, the first BPF SPL difference between the two configurations was estimated to be 17.8 dB [7] and is measured here as 17.5 dB. Moreover, the first four BPF harmonics differ by more than 10 dB between the two configurations. As noted by Soderman and Allen [20], a separation greater than 10 dB between the signal and background is desirable for assessing the noise sources as distinct.

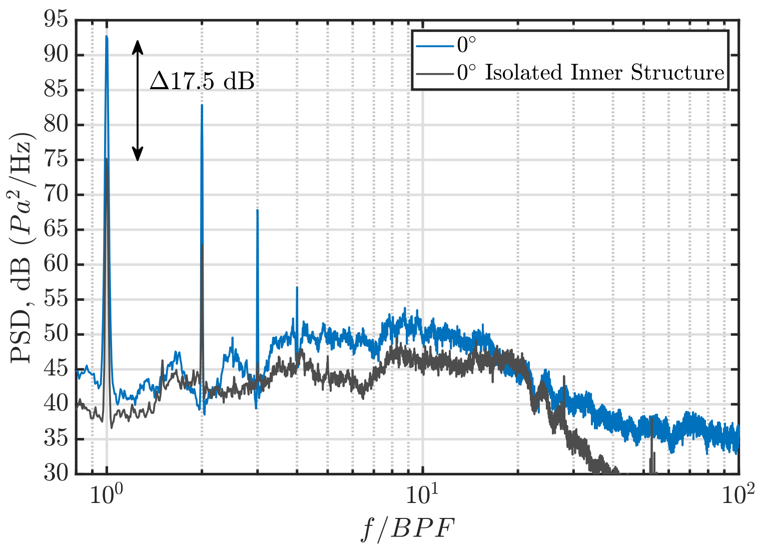

Fig. 12 Signal-to-noise ratio characterization with respect to theory-based Ω^4 thickness noise scaling estimate of 17.8 dB at the 0° microphone.

Having established that the measured response is governed primarily by the outer test section, Fig. 13 characterizes TUC-TUC's 1st BPF scaling behavior with rotational velocity. Canonically, compact low-Mach-number monopole-, dipole-, and quadrupole-type aeroacoustic sources scale in far-field mean-square pressure at fixed observer geometry, as Ω^4, Ω^6, and Ω^8, respectively; the quadrupole Ω^8 scaling follows from Lighthill's acoustic analogy [21], while the lower-order surface-source terms are associated with the boundary extensions of Curle and Ffowcs Williams–Hawkings [22, 23]. When a moving source is considered, velocity scalings also depend on blade and harmonic number. For this case, where $mB = 2$, the corresponding lift-, drag-, and thickness-noise contributions scale as Ω^{10}, Ω^{8}, and Ω^{8}, respectively [9, 18, 24]. Therefore, given the relatively large thickness of the TUC-TUC blade sections, and the relatively low loading noise contributions demonstrated in the following figures, the measured velocity dependence falls near an Ω^{8} scaling. Taken together, Figs. 12 and 13 demonstrate that the baseline acoustic response of TUC-TUC is consistent with the acoustic-theory-based design assumptions [7] and that the contribution of the inner structure remains sufficiently separated from that of the outer test section for meaningful acoustic characterization.

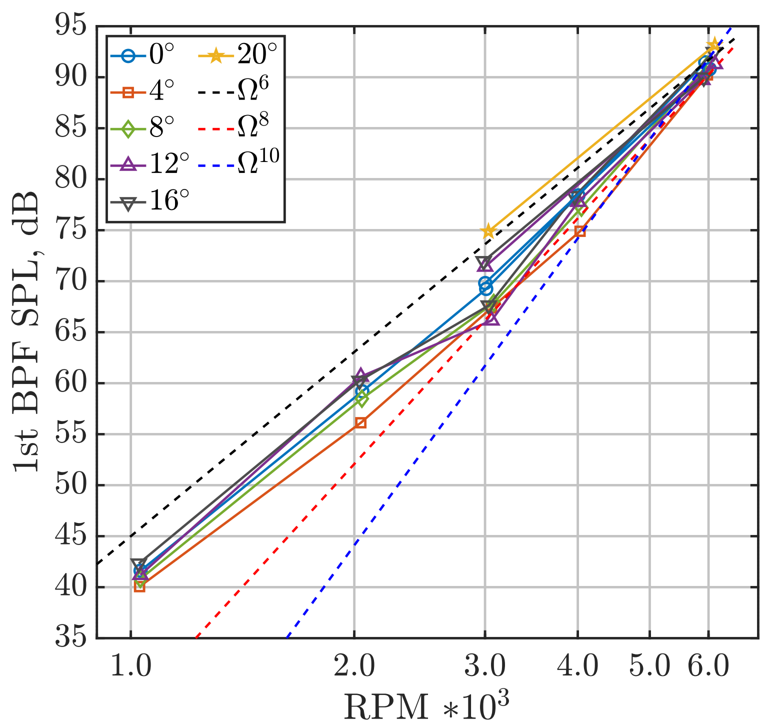

Fig. 13 Measured 1st BPF SPL across varying angles and speeds for the 40° microphone, compared with different velocity power scalings.

Figure 14 presents the measured and estimated harmonic-isolated SPL at the 40° microphone for varying pitch angles at ~6,000 RPM. At 0° pitch, the measured and estimated BPF SPLs exhibit the expected monotonic decay with increasing harmonic number. At higher pitch angles, the measured response maintains a general decrease with harmonic number, but this decay is no longer strictly monotonic over the first several harmonics. Meanwhile, the 1st BPF generally increases with pitch angle, consistent with the increasing influence of loading-related tonal contributions. This trend is reflected in both the measurements and the estimates. The 16° pitch case departs slightly from this trend; however, the deviation is comparable to the microphone precision and therefore could reflect either a physical effect or measurement scatter. In contrast, the estimated higher harmonics continue to decay monotonically, whereas the measured response shows a more irregular harmonic distribution beyond the 2nd BPF. Further investigation is needed to determine whether this higher-harmonic non-monotonicity arises from aerodynamic effects, measurement limitations, or both.

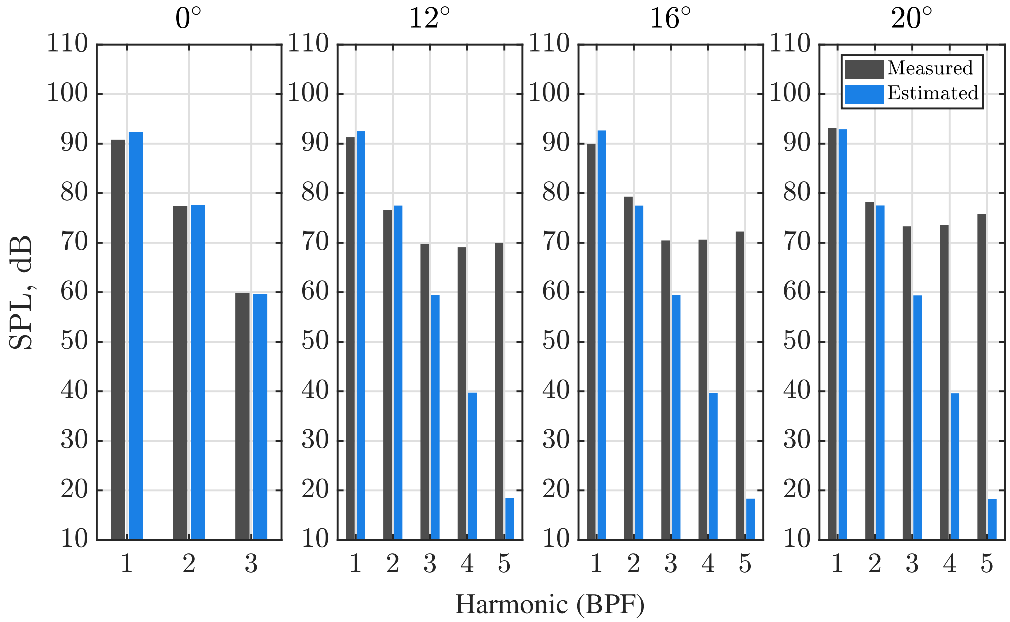

Fig. 14 SPL harmonic comparison of varying pitch angle at 6,000 RPM at the 40° microphone.

Figures 15 - 18 show the measured and estimated directivity of the tonal OASPL for varying pitch angles at ~6,000 RPM. For clarity, downwards in the plot is the positive thrust direction, as marked by the arrow. Generally, the measured tonal OASPL does not vary greatly in magnitude across the microphone range and is congruent with the trends demonstrated by the predictions. Table 6 summarizes the measured and estimated SPL, per noise source component, per test case. The respective measured value is also reported for comparison. Given the ±1 dB accuracy of the microphones, good quantitative matching of the measurements and estimates are demonstrated. Evidently, the thickness noise dominates the total response. Variation in pitch – and therefore in loading noise – was expected to yield a measurable change in the acoustic response. However, the measured results do not show a clearly distinguishable loading-noise contribution for the pitch angles assessed. Using the estimates as context for inferring the experimental response, it becomes clear that measured noise "hides" the influence of loading noise, due to the high thickness noise contribution. Even at the highest pitch angle considered, the summation of the estimated thickness- and loading-noise sources does not substantially modify the total noise. Further testing at higher pitch angles in addition to future analysis aimed at separating loading noise from thickness noise via only the measurements will be explored.

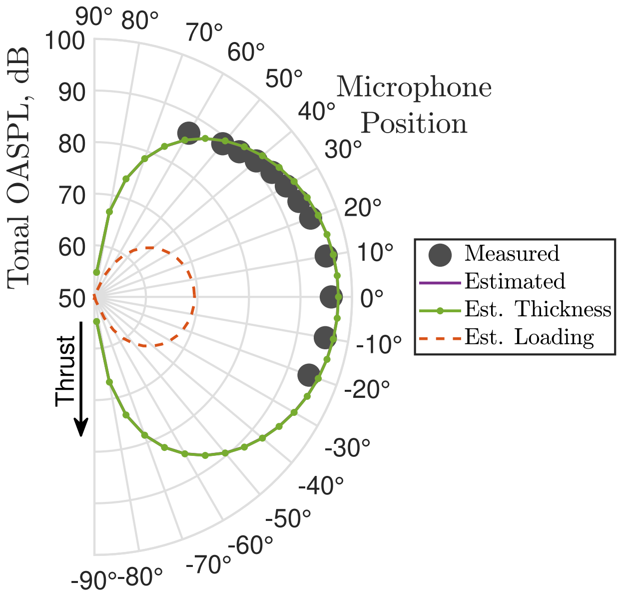

Fig. 15 **0° pitch OASPL at 6000 RPM.**

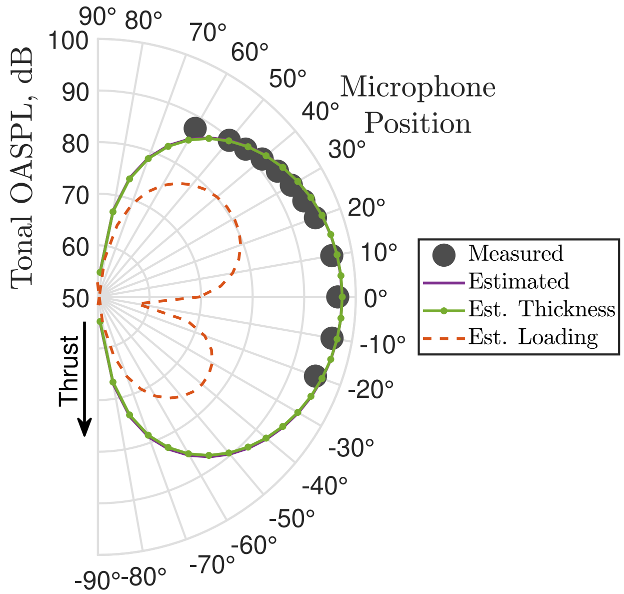

Fig. 16 **12° pitch OASPL at 6000 RPM.**

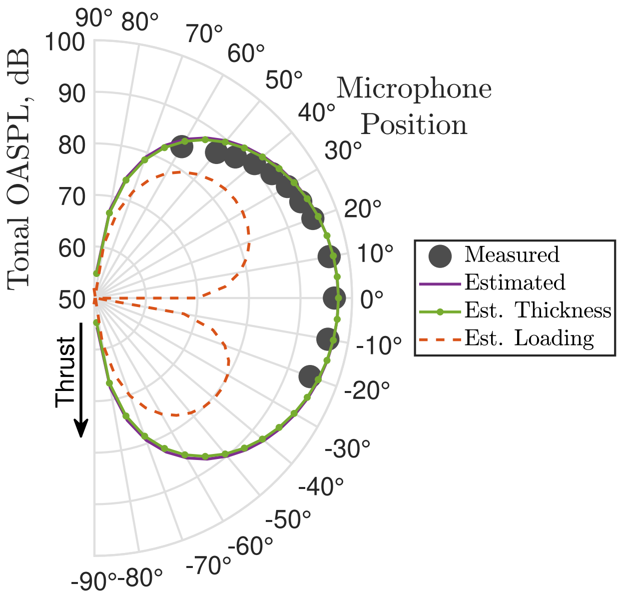

Fig. 17 **16° pitch OASPL at 6000 RPM.**

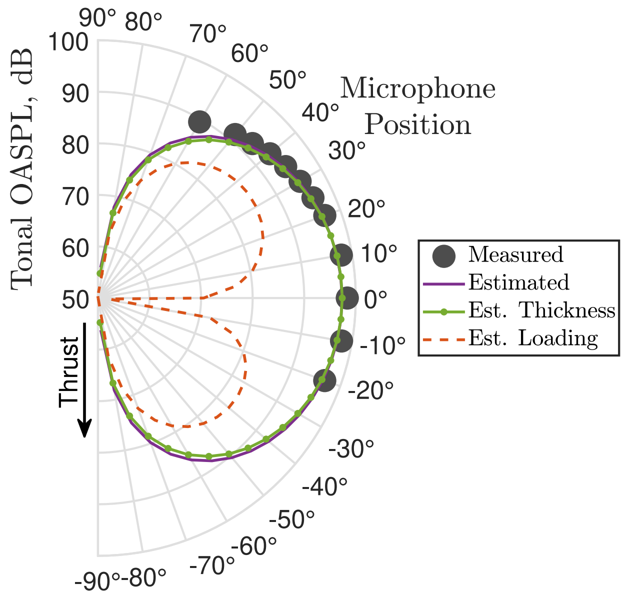

Fig. 18 **20° pitch OASPL at 6000 RPM.**

Table 6 **Thickness and loading OASPL estimates at 6000 RPM for the 40° microphone.**

Pitch Angle [deg]	Thickness Noise [dB]	Loading Noise [dB]	Total Noise [dB]	Measured Noise [dB]
0	92.6	64.8	92.6	91.0
12	92.6	80.1	92.6	91.6
16	92.6	83.0	92.8	90.6
20	92.6	85.2	93.0	93.5

Figure 19 shows the measured spectra for several test cases at the 0° microphone, and Fig. 20 shows just the broadband frequency range of the spectra. Since operation at 0° pitch represents a special case in which the blades consistently ingest their own wake, this condition also exhibits the highest average broadband levels. Relative to the isolated inner-structure configuration, the broadband spectrum differs by ~15 dB at high frequencies, further supporting the notion of the separation of sources for the inner to full TUC-TUC testing configuration. Moreover, the difference in broadband signal is notably more pronounced between 16° to 20° compared to 12° to 16°, which may be due to a change in boundary layer state. The spectral peak at frequencies slightly above 10^4 Hz is attributed to motor noise, consistent with the motor's electronic switching frequency.

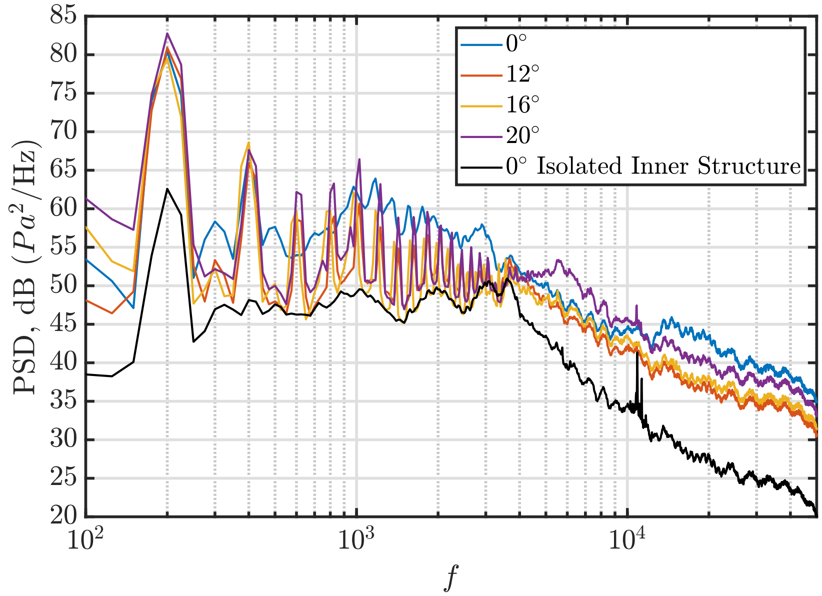

Fig. 19 Spectra comparison at the 0° microphone. The spectra were processed with a Welch autocorrelation block size of 4,096, a Hanning window and 0.5 overlap window.

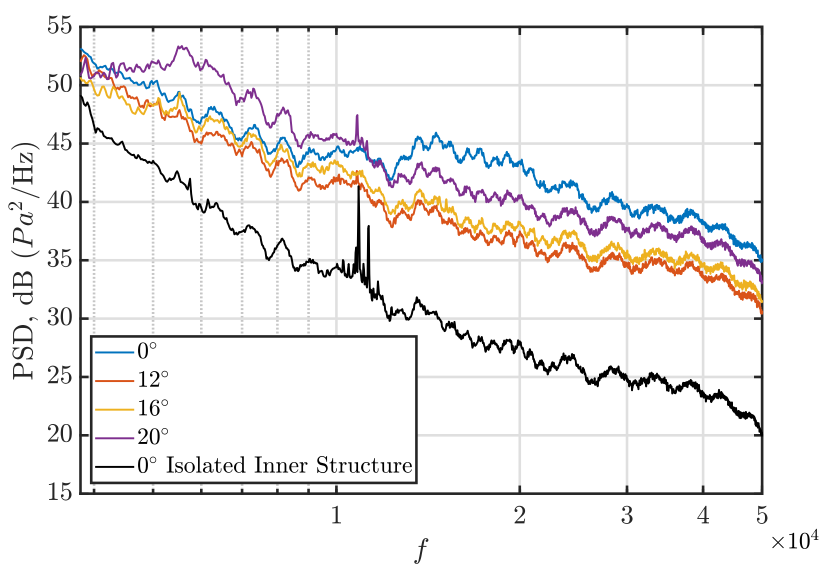

Fig. 20 Broadband spectra comparison at the 0° microphone. The spectra were processed with a Welch autocorrelation block size of 4,096, a Hanning window and 0.5 overlap window.

V. Conclusion and Future Work

This work presented the commissioning and initial hover characterization of TUC-TUC, a simplified rotor aeroacoustic test bench developed to support the study of rotor-noise mechanisms under more controlled and interpretable conditions than are typically possible with conventional rotor geometries. The experimental methodology combined integral load measurements, particle image velocimetry, and acoustic directivity measurements, while simplified physics-based prediction methods were used to provide a basis for comparison with the measured response. In this way, the present study assessed both the functionality of the platform and its suitability for future aerodynamic and aeroacoustic investigations.

The measured rotor performance demonstrated the expected trends for thrust and torque, albeit at low loading conditions, where deviations occured. Although an offset of approximately 1–2° is present between the predicted and measured datasets, the overall agreement in the magnitude and trend of the aerodynamic response indicates that the underlying model physics are captured reasonably well by the BEMT model. This supports the use of the model, within its limits, for the design performed and future study of TUC-TUC, while the source of the offset remains to be determined. In addition, PIV-based flow-field analysis at the test-section mid-plane suggested that the local flow could be treated as quasi-2D, consistent with corresponding 2D sectional performance estimates for the same operating condition.

The measured acoustic response was likewise found to be broadly consistent with the intended design criteria. Thickness noise dominated the overall response and followed the expected eighth-power velocity scaling. Additionally, the signal-to-noise ratio between the outer and inner sections was within 0.3 dB of the prediction. The harmonic response also showed the expected overall decrease in SPL with increasing BPF harmonic, as reflected in both the measurements and the estimates. At the same time, the measured harmonic decay was not strictly monotonic over the first few harmonics, indicating a more complex higher-harmonic structure than that captured by the present prediction approach. The first and second BPF SPL predictions agreed with the measurements to within approximately 2 dB, whereas the higher harmonics exhibited larger deviations.

Taken together, these results show that TUC-TUC provides a suitable basis for controlled aerodynamic and aeroacoustic characterization, while also identifying several areas for continued study. Ongoing work is focused on resolving the apparent pitch-angle mismatch between prediction and experiment, extending the test envelope to higher blade-pitch conditions, and further assessing pitch-dependent changes in loading-noise response, including separation of loading-noise and thickness-noise contributions from the measured signal. More broadly, the present results position TUC-TUC as a platform for follow-on studies of rotor aeroacoustics, including unsteady loading effects, the influence of airfoil variation, and the characterization of broadband-noise generation under controlled conditions. The platform therefore provides a foundation for more detailed investigation of the mechanisms governing rotor-noise radiation and their comparison with analytical and physics-based prediction methods.

Appendix A: Load Measurement Reduction and Uncertainty Quantification

The thrust and torque signals were converted from voltage to physical units using the manufacturer-provided calibration. Uncertainty quantification followed the GUM framework and AIAA's practices on experimental uncertainty assessment [25–28]. The uncertainty quantification combines Type A and Type B standard uncertainties by root-sum-square and reporting expanded uncertainty at approximately 95% confidence. For each acquisition, the signal was divided into `PRE`, `MAIN`, and `POST` segments, where `PRE` and `POST` were non-rotating tare measurements obtained before and after the run. A drift-aware tare was constructed by linearly interpolating between the pre- and post-run baseline means,

$$T_0(t) = \bar{T}_{\mathrm{pre}} + \left(\bar{T}_{\mathrm{post}} - \bar{T}_{\mathrm{pre}}\right) \frac{t - t_{\mathrm{pre}}}{t_{\mathrm{post}} - t_{\mathrm{pre}}}, \qquad Q_0(t) = \bar{Q}_{\mathrm{pre}} + \left(\bar{Q}_{\mathrm{post}} - \bar{Q}_{\mathrm{pre}}\right) \frac{t - t_{\mathrm{pre}}}{t_{\mathrm{post}} - t_{\mathrm{pre}}}, \tag{A1}$$

and subtracted from the full thrust and torque records prior to averaging.

The reported measurand was the mean of the corrected signal over `MAIN(trim)`, obtained by removing 1 s from the beginning and end of `MAIN`. Type A uncertainty was estimated from the scatter of 10-revolution block means, with an effective sample size correction applied to account for serial correlation. The tare uncertainty was estimated from the `PRE` and `POST` segments and propagated through the interpolation in Eq. A1. Type B uncertainty included manufacturer-based load-cell and amplifier contributions, namely nonlinearity, hysteresis, non-repeatability, temperature-induced zero and span effects, amplifier nonlinearity, and amplifier drift, when available. Bounded specification terms were treated as rectangular distributions and converted to standard uncertainties by division by $\sqrt{3}$ [25, 26]. A conservative temperature drift of $\Delta T = 5°\mathrm{C}$ was assumed despite the use of a constant temperature, chilled water heat sink integration plate between the motor and load cell. A calibration-fit term proportional to the reported mean load was also included.

The combined standard uncertainty was computed as

$$\epsilon_c = \sqrt{\epsilon_A^2 + \epsilon_{\text{tare}}^2 + \epsilon_{\text{cal}}^2 + \epsilon_B^2}, \tag{A2}$$

and the expanded uncertainty is reported as

$$\varepsilon_{95} = k_{95}\epsilon_c, \tag{A3}$$

where the effective degrees of freedom were estimated using the Welch-Satterthwaite relation, and k_{95} was obtained accordingly when available, with fallback to $k = 2$. The reported thrust and torque coefficients correspond to the drift-corrected means over `MAIN(trim)` with their associated 95% expanded uncertainties.

The uncertainty in figure of merit was obtained by propagation of the coefficient uncertainties in C_T and C_Q. Assuming C_T and C_Q to be uncorrelated because the FUTEK load cell possess limited channel cross-talk, the standard uncertainty in FM was evaluated from the first-order Taylor-series propagation shown in Eq. A4,

$$\epsilon_{FM} = |FM|\sqrt{\left(\frac{3}{2}\frac{\epsilon_{C_T}}{C_T}\right)^2 + \left(\frac{\epsilon_{C_Q}}{C_Q}\right)^2}. \tag{A4}$$

The corresponding expanded uncertainty was then reported as $\varepsilon_{FM,95} = k_{95}\epsilon_{FM}$, using the same coverage-factor convention described previously.

Acknowledgments

The authors gratefully acknowledge Yannick Chance for his time and support assisting with the experiments described; Kangni Combey for his support and assistance; Wouter Gregor of TU Delft Demo for his design engineering and analysis work; Emiel Langedijk and Stefan Bernardy for their technical support; and Till Lidner, Jens Friedsrich and Daniel Kessler of TU Branuschweig for their support lending hardware.

References

[1] d. Monteiro, F., Merino-Martínez, R., and Pereira, L. T. L., "Psychoacoustic Evaluation of an Array of Distributed Propellers Under Synchrophasing Operation," *30th AIAA/CEAS Aeroacoustics Conference*, 2024. https://doi.org/10.2514/6.2024-3321.

[2] Chai, Z., Liu, X., and Yu, H.-D., "Numerical Study on Dual-Rotor Phase Synchronization for Tonal Noise Counteraction," *Aerospace Research Communications*, Vol. 2, No. 1, 2025, p. 15262. https://doi.org/10.3389/arc.2025.15262.

[3] Wickersheim, R., Keßler, M., and Krämer, E., "Numerical Investigation and Validation of Noise Sources of a Distributed Propulsion System," *AIAA Journal*, Vol. 63, No. 4, 2025, pp. 1418–1430. https://doi.org/10.2514/1.J064531.

[4] Groom, M. J., Zhou, J., and Lopes, L. V., "Numerical Investigation of Propeller–Wing Interaction Noise with Scattering and Shielding," *AIAA AVIATION 2025 Forum*, 2025. https://doi.org/10.2514/6.2025-3369.

[5] Rendón-Arredondo, J., Vella, E., Arroyo Ramo, A., Roger, M., Gojon, R., Jardin, T., and Moreau, S., "Aeroacoustic Investigations of a Rotor–Beam Configuration in Small-Size Drones," *The Journal of the Acoustical Society of America*, Vol. 158, No. 2, 2025, pp. 1091–1102. https://doi.org/10.1121/10.0038975.

[6] Lima Pereira, L. T., Ragni, D., Romani, G., and Casalino, D., "Accuracy of Tonal Noise Prediction of Propellers via Numerical Simulations and Experimental Campaigns," *30th AIAA/CEAS Aeroacoustics Conference*, Rome, Italy, 2024. https://doi.org/10.2514/6.2024-3267, aIAA 2024-3267.

[7] Bensignor, I., Pereira, T., and Ragni, D., "TUC-TUC: Development of a Test Bench for the Study of Rotor Aeroacoustics," *Proceedings of the 54th International Congress and Exposition on Noise Control Engineering*, WTC Events Center, São Paulo, SP, Brazil, 2025. URL https://www.even3.com.br/anais/international-congress-exposition-noise-control-engineering/1076461-TUC-TUC--DEVELOPMENT-OF-A-TEST-BENCH-FOR-THE-STUDY-OF-ROTOR-AEROACOUSTICS.

[8] Magliozzi, B., Hanson, D. B., and Amiet, R. K., "Aeroacoustics of Flight Vehicles: Theory and Practice, Propeller and Propfan Noise, Vol. 1," Tech. Rep. NASA-RP-1258-VOL-1, NASA, 1991.

[9] Lowson, M. V., and Ollerhead, J. B., "Studies of Helicopter Rotor Noise," Final Report AD0684394, Wyle Labs, Research Staff, Huntsville, AL, Jan. 1969. URL https://apps.dtic.mil/sti/citations/AD0684394.

[10] Merino-Martínez, R., Rubio Carpio, A., Lima Pereira, L. T., van Herk, S., Avallone, F., Ragni, D., and Kotsonis, M., "Aeroacoustic design and characterization of the 3D-printed, open-jet, anechoic wind tunnel of Delft University of Technology," *Applied Acoustics*, Vol. Vol. 170, 2020, p. 107504. https://doi.org/10.1016/j.apacoust.2020.107504.

[11] Wadlin, K. L., Fontana, R. E., and Shuford, C. L., *The Effect of End Plate, End Struts, and Depth of Submergence on the Characteristics of a Hydrofoil*, NACA-RM-L51B13, 1951.

[12] J., L. G., *Principles of Helicopter Aerodynamics*, Cambridge University Press, 2006.

[13] "Mechanical vibration — Rotor balancing — Part 11: Procedures and tolerances for rotors with rigid behaviour," Tech. Rep. ISO 21940-11:2016, International Organization for Standardization, 2016. URL https://www.iso.org/standard/54074.html.

[14] Cai, J., and Gunasekaran, S., "Propeller Ground Effect in Forward Flight," *AIAA Journal*, Vol. 61, No. 10, 2023, pp. 4378–4390. https://doi.org/10.2514/1.J062984.

[15] Wu, H., Chen, W., Jiang, H., Zhong, S., and Zhang, X., "Experimental investigation of the effect of sectional airfoil profile deviation on propeller noise," *Physics of Fluids*, Vol. 35, No. 2, 2023, p. 027104. https://doi.org/10.1063/5.0135555.

[16] Raffel, M., Willert, C. E., Scarano, F., Kahler, C. J., Wereley, S. T., and Kompenhans, J., *Particle image velocimetry: A practical guide*, Springer, 2018.

[17] Welch, P. D., "The Use of Fast Fourier Transform for the Estimation of Power Spectra: A Method Based on Time Averaging Over Short, Modified Periodograms," *IEEE Transactions on Audio and Electroacoustics*, Vol. 15, No. 2, 1967, pp. 70–73. https://doi.org/10.1109/TAU.1967.1161901.

[18] Hanson, D. B., "Influence of propeller design parameters on far-field harmonic noise in forward flight," *AIAA Journal*, Vol. 18, No. 11, 1980, p. 1313–1319. https://doi.org/10.2514/3.50887.

[19] Goyal, J., ". Hanson's Model in Frequency Domain - Tonal Noise of Rotors in Uniform Inflow." , 2023. URL https://doi.org/10.4121/7da5aa45-e44b-4fa3-9407-8bf61e835d99.

[20] Soderman, P. T., and Allen, C. S., *Microphone Measurements In and Out of Airstream*, Springer Berlin Heidelberg, Berlin, Heidelberg, 2002. https://doi.org/10.1007/978-3-662-05058-3_1.

[21] Lighthill, M. J., "On Sound Generated Aerodynamically. I. General Theory," *Proceedings of the Royal Society of London. Series A. Mathematical and Physical Sciences*, Vol. 211, No. 1107, 1952, pp. 564–587. https://doi.org/10.1098/rspa.1952.0060.

[22] Curle, N., "The Influence of Solid Boundaries upon Aerodynamic Sound," *Proceedings of the Royal Society of London. Series A. Mathematical and Physical Sciences*, Vol. 231, No. 1187, 1955, pp. 505–514. https://doi.org/10.1098/rspa.1955.0191.

[23] Ffowcs Williams, J. E., and Hawkings, D. L., "Sound Generation by Turbulence and Surfaces in Arbitrary Motion," *Philosophical Transactions of the Royal Society of London. Series A, Mathematical and Physical Sciences*, Vol. 264, No. 1151, 1969, pp. 321–342. https://doi.org/10.1098/rsta.1969.0031.

[24] Hanson, D. B., and Parzych, D. J., "Theory for Noise of Propellers in Angular Inflow with Parametric Studies and Experimental Verification," Contractor Report NASA-CR-4499, NASA, Mar. 1993. URL https://ntrs.nasa.gov/citations/19930015905.

[25] Joint Committee for Guides in Metrology, "Evaluation of Measurement Data—Guide to the Expression of Uncertainty in Measurement," Tech. Rep. JCGM 100:2008, JCGM, 2008. https://doi.org/10.59161/JCGM100-2008E.

[26] Taylor, B. N., and Kuyatt, C. E., "Guidelines for Evaluating and Expressing the Uncertainty of NIST Measurement Results," Tech. Rep. NIST Technical Note 1297, National Institute of Standards and Technology, Gaithersburg, MD, Sep. 1994. https://doi.org/10.6028/NIST.TN.1297.

[27] American Institute of Aeronautics and Astronautics, "Assessment of Experimental Uncertainty with Application to Wind Tunnel Testing," Tech. Rep. AIAA S-071A-1999, American Institute of Aeronautics and Astronautics, Reston, VA, 1999. https://doi.org/10.2514/4.107450.001.

[28] American Institute of Aeronautics and Astronautics, "Calibration and Use of Internal Strain-Gage Balances with Application to Wind Tunnel Testing," Tech. Rep. AIAA R-091A-2020, American Institute of Aeronautics and Astronautics, Reston, VA, 2020. https://doi.org/10.2514/4.106019.001.